Research Article | Vol. 27, No. 4 | 18 Feb 2019 | OPTICS EXPRESS 3920
Optics EXPRESS

Rapidly tunable orbital angular momentum (OAM) system for higher order Bessel beams integrated in time (HOBBIT)

WENZHE LI, KAITLYN S. MORGAN, YUAN LI, J. KEITH MILLER,* GRAHAM WHITE, RICHARD J. WATKINS, ERIC G. JOHNSON

Micro-Photonics Laboratory, the Holcombe Department of Electrical and Computer Engineering, Center for Optical Materials Science and Engineering Technologies (COMSET), Clemson University, Clemson, South Carolina, 29634, USA
*jkmill@clemson.edu

Abstract: Beams with fast and continuously-tunable orbital angular momentum (OAM) have potential applications in classical and quantum optical communications, sensing, and in the study of beam propagation through turbulence. An acousto-optical deflector (AOD) is a sophisticated, well-studied device that continuously and rapidly tunes the deflection angle of an output beam. The log-polar HOBBIT setup can generate beams with OAM by wrapping elliptically shaped Gaussian beams with linear phase tilt to a ring. By combining the linear tilted output from the AOD with the OAM generation capabilities of the HOBBIT system, the generated OAM modes become continuously tunable at high speeds measured on the order of 400 kHz.

1. Introduction

As interest in the exploration of orbital angular momentum (OAM) properties grows, fast switching between different OAM modes is a key technique needed to thoroughly explore applications. A common approach in both classical and quantum OAM communications uses different OAM modes as symbols or bits. The capability of switching or hopping between OAM modes can increase data rate dramatically [1–5]. Studies of OAM beams in turbulent environments suggests that different OAM modes have different propagation performances through turbulence [6,7]. Fast switching between OAM modes will benefit such studies by enabling the exploration of a wide range of OAM modes. Other sensing related applications that could benefit from rapidly-tunable OAM include beam steering through scattered media [8], particle manipulation using three dimensional beams [9], object rotation detection [10,11], temperature sensing [12], and motion detection [13].

So far, one of the most popular techniques for mode switching uses spatial light modulators (SLM), a device that has a very limited switching speed. Digital micro-mirror devices (DMD) can boost switching speeds up to tens of kHz [4], which is comparable with the switching speed of a direct OAM mode emitter [14]. The DMD micro-mirror pitch limits the spatial resolution, while the mode emitter is only capable of tuning integer OAM modes. Fractional OAM modes, also referred to as non-integer [15], continuous [16], successive [16], and rational [17] modes are another interesting aspect of study. This is primarily because it is almost impossible to generate an entirely pure integer OAM state. Secondly, it has been analytically deduced that fractional OAM Bessel beams could form an infinite number of orthogonal subsets of OAM modes [18], which can further benefit classical and quantum optical communication. Thirdly, the fractional OAM Bessel beams preserve the non-diffracting properties that integer OAM beams possess [16]. This property is key for beam propagation applications, including propagation through turbulence and turbid environments. Moreover, it has been found that a group of fractional OAM modes generated by a synthesis

#350075 https://doi.org/10.1364/OE.27.003920
Journal © 2019 Received 8 Nov 2018; revised 19 Dec 2018; accepted 20 Dec 2018; published 4 Feb 2019

Optics EXPRESS

of Laguerre-Gaussian (LG) modes have good structural stability on propagation to the far field [19]. These LG mode-based fractional OAM states can be used in both classical and quantum communication.

The proposed fast tunable OAM generation technique utilizes an optical geometric transformation [20–23] known as the log-polar transform [24–33]. Refractive log-polar elements were first explored as an efficient OAM mode sorter in 2010 [24]. In 2013, Mirhosseini used a fan-out diffractive beam-copying method to increase the log-polar mode sorter separation efficiency up to 95% [27]. In 2013, Mhlanga successfully sorted more than forty HeNe Bessel beam OAM modes. In 2015, the same elements were successfully used to demultiplex OAM modes with higher mode selectivity and better efficiency than that of cascaded beam splitters [25]. In 2015, Morgan designed and fabricated a diffractive version of the log-polar elements for OAM mode (de)multiplexing [33]. In 2016, Srimathi used the same log-polar elements for an underwater communication link [28]. In 2017, Ruffato made a compact demultiplexing version of the log-polar elements operating at 632.8 nm [30,31]. In 2017, Lightman 3D printed a log-polar mode sorter, which working for a broad-spectrum of light [32]. In 2018, Ruffato redesigned the log-polar diffractive elements and explored the non-paraxial regime property, which is a good example of diffractive device miniaturization [34].

The acousto-optical deflector (AOD) is a reasonably fast modulation device that is commonly used for stable phase modulation and beam shaping [35]. Bessel beams have been generated using an AOD array [36] and a cylindrical axisymmetric AOD [37]. In this work, a novel technique for OAM switching and tuning using an AOD in conjunction with a log-polar coordinate transformation system is demonstrated. The maximum mode switching speed for the experimental setup is measured on the order of 400 kHz, which is determined by the acoustic velocity of the crystal as well as the beam diameter. For a different AOD and a reduced beam size, this speed has the potential of reaching tens of MHz with sub-microsecond response time — far higher than the kHz level switching methods mentioned above. Typically, AODs have a very high damage threshold and are widely used in high power laser systems for beam deflecting and laser pulse generation. The integration of an AOD also opens up high power and direct energy related applications for our HOBBIT system.

2. Method

The two log-polar coordinate transform optics work as a pair to perform the optical transformation of wrapping a linear-distributed beam into an annular-distribution. The mapping process involves two customized diffractive phase optics: the wrapper which performs the line to ring transformation, while the phase-corrector corrects the phase distortion introduced by the wrapper upon propagation. Interestingly, if a length-wise linear phase is applied along the linear-distributed beam, this will be transformed as well, producing a spiral phase which has been encoded onto the wrapped-ring. Therefore, the far field of this ring shape beam carries OAM.

As the basis of this work, the optical setup used to generate OAM modes is shown in Fig. 1(a). In this technique, a Gaussian input beam is passed through an AOD. When a voltage signal with the central frequency of the AOD is applied, the 1st order deflection of the Gaussian input is at the Bragg condition with the Gaussian beam propagating along the optical axis. In this orientation, the Gaussian beam has a flat wavefront and the designed system will generate an OAM mode of charge equal to zero. When the frequency of the acoustic wave deviates from this center frequency, the beam is instead deflected by some additional angle along the horizontal direction as shown in Fig. 1(a). The deviation away from the Bragg condition results in the 1st order deflection with a tilted phase relative to the axis of propagation. The output of the AOD is then passed through a 4-*f* embedded line generator, used as a dual-axis manipulator. The output of the 4-*f* embedded line generator is an elliptical

Optics EXPRESS

beam with an elongated length and a suppressed height with a phase tilt along the horizontal direction specific to the applied acoustic frequency. This elliptical beam then propagates through the log-polar HOBBIT optics that wrap the ellipse into an asymmetric annular-distribution. Overall, this results in an elliptical Gaussian beam with linear phase being wrapped into an asymmetric ring with azimuthal OAM phase, which is the angular spectrum of the asymmetric Bessel-Gauss beams. The seminal concept of asymmetric Bessel beams and its physically realistic version, asymmetric Bessel-Gauss beams, have been proposed and studied by Kotlyar in 2014 [38,39]. In 2018, a general case of asymmetric Mathieu beams has been analytically derived and experimentally generated by Barcelo-Chong, who showed the recovery of asymmetric Bessel modes when the ellipticity parameter approaches zero [40]. Bessel-Gauss beams are well known for their nondiffracting behavior, but this property relies on the size of the Gaussian envelope. A larger Gaussian envelope produces more ringing, which in turn produces the longer Rayleigh range. In this case, a small Gaussian envelop is used, which will reduce the nondiffracting behavior. In addition, the azimuthal distribution of the angular spectrum of the asymmetric Bessel-Gauss beams is different from Kotlyar's papers [38,39], which will be discussed in detail later in this paper.

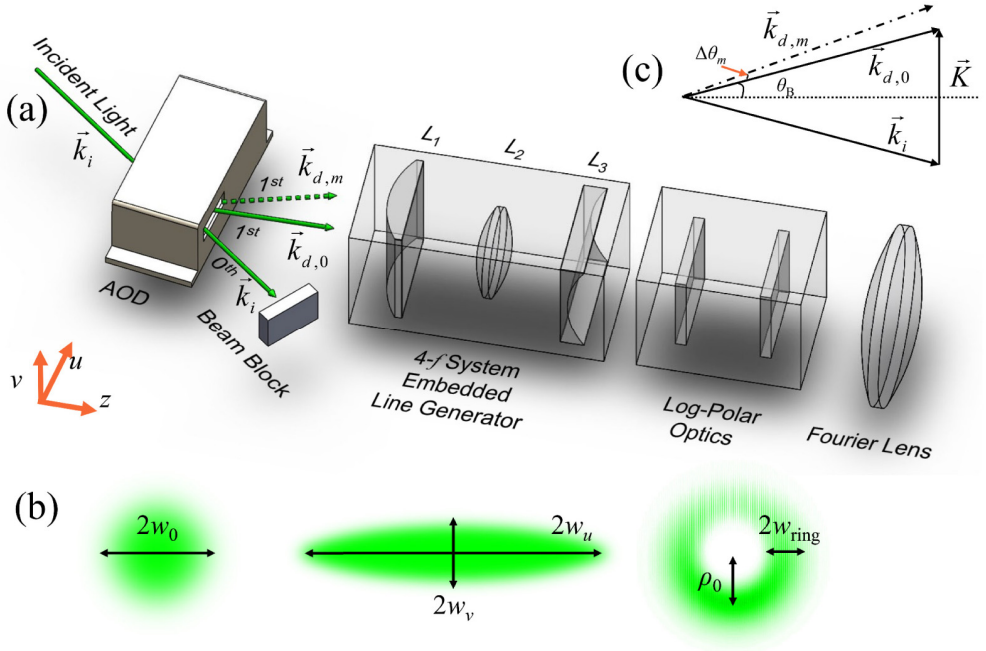

Fig. 1. (a) The proposed AOD concept, (b) illustration of the beam profiles at the AOD, after the line generator and after the log-polar optics and (c) the momentum vector diagram.

The input to the AOD has a Gaussian distribution with the diameter of the beam defined as $2w_0$ as shown in Fig. 1(b). The momentum vector of incident photon is $\vec{k}_i$, that of the diffracted photon is $\vec{k}_d$, and that of the phonon is $\vec{K}$. According to the principle of momentum conservation, the momentum vector of the diffracted photon should be equal to the sum of the momentum vectors of the incident photon and of the acoustic phonon, $\vec{k}_d = \vec{k}_i + \vec{K}$, shown in Fig. 1(c). The notation $\vec{k}_{d,0}$ and $\vec{k}_{d,m}$ is used for the diffracted photon's momentum vector when the far-field beam has charge 0 and m, respectively. The OAM mode index $m = l + \alpha$ is a continuous charge number in which l is the integer part and α is the fractional part, which is defined as a positive real number $0 \le \alpha < 1$. The Bragg angle is greatly

Optics EXPRESS

exaggerated in Fig. 1(a) for visual clarity, and a general Bragg angle equation can be represented as

$$\theta_{\mathrm{B}} \cong \sin\left(\theta_{\mathrm{B}}\right) = \frac{\left|\vec{K}\right|}{2\left|\vec{k}_i\right|} = \frac{\lambda_0 f_0}{2V_{\mathrm{a}}}, \tag{1}$$

Where λ_0 is the electromagnetic wave Doppler shifted wavelengths corresponding to the OAM charge 0, V_{a} is the acoustic velocity and f_0 is the driving frequency of the AOD that results in the Bragg condition, and it's also the frequency corresponding with charge 0 output. The 1st order diffractive angle is $2\theta_{\mathrm{B}}$. By deviating the applied frequency away from the Bragg condition, $\Delta f_{\mathrm{m}} = |f_0 - f_{\mathrm{m}}|$, where f_{m} is the AOD driving frequencies corresponding with charge m output, there is a change in the deflection angle of the beam for charge m as

$$\Delta\theta_m = \left|\theta_m - \theta_0\right| = \left|\frac{\lambda_m \cdot f_m}{V_{\mathrm{a}}} - \frac{\lambda_0 \cdot f_0}{V_{\mathrm{a}}}\right| \approx \frac{\lambda_m \cdot \left|f_m - f_0\right|}{V_{\mathrm{a}}} = \frac{\lambda_m \cdot \Delta f_m}{V_{\mathrm{a}}}, \tag{2}$$

where λ_m is the electromagnetic wave Doppler shifted wavelengths corresponding to the OAM charge m. Since these wavelengths are extremely close with each other, differing by femtometers for a 532 nm input signal, we assume $\lambda_m \approx \lambda_0$. The angle deviation after the line generator, $\Delta\theta_m'$, will be scaled by the magnification of the 1st 4-f system according to

$$\Delta\theta_m' = \Delta\theta_m \frac{F_1}{F_2}, \tag{3}$$

where F_1 and F_2 are the focal lengths of the lenses L_1 and L_2, respectively, in Fig. 1. According to the paraxial approximation, this angle deviation corresponds to charge m and can be represented by

$$\Delta\theta_m' \approx \tan\left(\Delta\theta_m'\right) = \frac{\lambda_m m}{2\pi a}, \tag{4}$$

where parameter a is one design parameter of the optics which controls the active area in which the line to ring transform is performed in the wrapping procedure. The length of the active area is $2\pi a$, where any portion of a beam that exceeds this length will not be transformed and therefore the corresponding power is lost. Combining Eqs. (2)–(4) results in an expression for charge m as a function of the frequency change from the Bragg condition given by

$$m = \frac{2\pi a\left(\Delta f_m\right) F_1}{V_{\mathrm{a}} F_2}. \tag{5}$$

As shown in Fig. 1, the 1st order deflected beam exiting the AOD is a Gaussian distribution, which can be expressed as

$$\begin{aligned} U_{\mathrm{AOD\_1st}}(u,v) &= \exp\left[-\frac{\left(u^2+v^2\right)}{w_0^{\,2}}\right]\exp\left[\mathrm{i}\left(2\pi\left(f_{\mathrm{c}}+f_m\right)t - \vec{k}_{d,m}\cdot\vec{r}\right)\right] \\ &= \exp\left[-\frac{\left(u^2+v^2\right)}{w_0^{\,2}}\right]\exp\left[\mathrm{i}\left(2\pi\left(f_{\mathrm{c}}+f_m\right)t - k_z z - k_u u\right)\right]. \end{aligned} \tag{6}$$

where u and v are both Cartesian coordinates, f_{c} is the input laser's central frequency, $k_z = 2\pi\cos\left(\Delta\theta_m\right)/\lambda_m$ and $k_u = 2\pi\sin\left(\Delta\theta_m\right)/\lambda_m \approx 2\pi\Delta\theta_m/\lambda_m$ are the wavenumbers along the

Optics EXPRESS

z and u direction, and finally $(f_c + f_m)$ and λ_m are the electromagnetic wave Doppler shifted frequency and wavelength corresponding to the OAM charge m. After passing through the AOD, the beam is sent to the line generator to be shaped into an elliptical Gaussian distribution using lenses L_1, L_2 and L_3 with focal lengths F_1, F_2 and F_3, respectively. The elliptical Gaussian beam now has diameters in both dimensions, defined as $2w_v = 2w_0F_3/F_2$ and $2w_u = 2w_0F_2/F_1$. The elliptical beam can be expressed as

$$U_{\text{line}}(u,v) = \exp\left[-\left(\frac{u^2}{w_u^{\,2}} + \frac{v^2}{w_v^{\,2}}\right)\right]\exp\left[\mathrm{i}\left(2\pi\left(f_c + f_m\right)t - k_z' z - k_u' u\right)\right]. \quad (7)$$

where the wavenumber along z direction is $k_z' = 2\pi\cos\left(\Delta\theta_m'\right)/\lambda_m = 2\pi\cos\left(\Delta\theta_m F_1/F_2\right)/\lambda_m$, and the wavenumber along u direction is $k_u' = 2\pi\Delta\theta_m'/\lambda_m = m/a$.

The elliptical Gaussian beam is then incident on the log-polar optics which have been well studied [24,25,41,42]. The HOBBIT mapping process uses two customized log-polar optics: the wrapper that maps the elliptical Gaussian beam to an asymmetric ring profile, and the phase-corrector that corrects the phase distortion introduced by the wrapper. Since the elliptical line has a horizontal Gaussian distribution, the HOBBIT system wraps it into an asymmetric ring with a ring radius, ρ_0, defined from the origin to peak intensity location and width, $2w_{\text{ring}}$, as shown in Fig. 1(c). Given the log-polar mapping equation of $u = a\arctan\left(y/x\right) = a\phi$, the near-field output from the proposed HOBBIT system is given by

$$U_{\text{near}}(\rho,\phi) = \exp\left[-\left(\frac{\left(\rho-\rho_0\right)^2}{w_{\text{ring}}^{\,2}} + \frac{\phi^2}{\left(\beta\pi\right)^2}\right)\right]\exp\left[\mathrm{i}\left(-m\phi + 2\pi\left(f_c + f_m\right)t - k_z' z\right)\right], \quad (8)$$

where ρ and ϕ are both the radial and azimuthal polar coordinates in the near-field plane, $\rho_0 = b\exp\left(-v_0/a\right)$ is the wrapped ring's radius defined from the origin to peak intensity location, $w_{\text{ring}} = b\left[\exp\left(-\left(v_0 - w_v\right)/a\right) - \exp\left(-\left(v_0 + w_v\right)/a\right)\right]/2$ is the wrapped ring's half width, v_0 is the input elliptical Gaussian beam's offset from the center of the wrapper, $w_v = w_0F_3/F_2$ is the half width of the input elliptical Gaussian beam, a is the log-polar optics design parameter which scales the transformed line length in unwrapping procedure, b is another log-polar optics design parameter which scales the transformed ring size in the wrapping procedure. This parameter is proportional to the wrapped ring radius, ρ_0. And finally $\beta = w_0F_2/(\pi aF_1)$ is the ratio of input elliptical Gaussian line's length to the designed input line length $2\pi a$. The Fourier transform of Eq. (8) can then be derived as

$$U_{\text{far}}(r,\theta) = A\exp\left(-\frac{r^2}{w_G^{\,2}}\right)\exp\left[\mathrm{i}\left(2\pi\left(f_c + f_m\right)t - k_z' z\right)\right]\sum_{n=-\infty}^{\infty} B_n \exp\left(\mathrm{i}n\theta\right) J_n\left(\frac{2\pi\rho_0}{\lambda_m F}r\right), \quad (9)$$

where r and θ are both the radial and azimuthal polar coordinates in the far field plane, $A = -w_{\text{ring}}^{\,2}\beta\pi^{5/2}\rho_0/\left(2\lambda f\right)$, $w_G = \lambda_m F/\left(\pi w_{\text{ring}}\right)$, F is the focal length of the Fourier lens, $B_n = \left(-\mathrm{i}\right)^{n-1} 2\exp\left[-\beta^2\pi^2\left(l + \alpha - n\right)^2/4\right]\mathrm{Im}\left[\mathrm{erfi}\left(\mathrm{i} + \beta\pi\left(l + \alpha - n\right)/2\right)\right]$, erfi($x$) = erf(i$x$)/i is the imaginary error function, and finally Im(z) gives the imaginary part of complex number z. As one can tell, the far-field of the ring shaped beam in Eq. (9) is the combination of a group of Bessel-Gaussian (BG) beams carrying OAM. Intuitively, it is a weighted linear combination of every possible integer OAM phase carrying n^{th}-order Bessel function of the 1$^{\text{st}}$ kind modulated by the same Gaussian envelop. The parameter B_n is the weighting or selection factor, which distributes the power within the central 2 to 3 modes and decays rapidly as m

Optics EXPRESS

approaches positive and negative infinity. When $\alpha = 0$, then $m = l$, meaning an integer charge will be select as $n = l$, and B_l is the maximum value. As α increases, the central weighting factor B_n's maximum value will move from $n = l$ to $n = l + 1$. This means fractional-charged OAM-carrying BG beams are a linear combination of integer BG beams. Considering the $\alpha = 0$ case, the B_n parameter has the property of

$$B_{m-k} = (-1)^k B_{m+k}, k = 0, 1, 2, \cdots \tag{10}$$

The far-field complex amplitude described by Eq. (9) can be rewritten as

$$\begin{aligned} U_{\text{far}}(r,\theta) = A\exp\left(-\frac{r^2}{w_{\text{G}}{}^2}\right)\exp\left[\text{i}\left(m\theta + 2\pi\left(f_m + f_{\text{c}}\right)t - k_z' z\right)\right] \\ \cdot\Bigg\{ \begin{aligned} &B_m J_m\left(\frac{2\pi\rho_0 r}{\lambda_m F}\right) \\ &+\text{i}\sin\theta\frac{m\lambda_m F}{\pi\rho_0 r}B_{m+1}J_m\left(\frac{2\pi\rho_0 r}{\lambda_m F}\right) \\ &+\cos\theta B_{m+1}\left[J_{m+1}\left(\frac{2\pi\rho_0 r}{\lambda_m F}\right) - J_{m-1}\left(\frac{2\pi\rho_0 r}{\lambda_m F}\right)\right] \\ &+\sum_{k=1}^{\infty}\Bigg\{ \begin{aligned} &B_{m+2k+1}\Bigg\{ \begin{aligned} &\cos\left((2k+1)\theta\right)\left[J_{m+2k+1}\left(\frac{2\pi\rho_0 r}{\lambda_m F}\right) - J_{m-2k-1}\left(\frac{2\pi\rho_0 r}{\lambda_m F}\right)\right] \\ &+\text{i}\sin\left((2k+1)\theta\right)\left[J_{m+2k+1}\left(\frac{2\pi\rho_0 r}{\lambda_m F}\right) + J_{m-2k-1}\left(\frac{2\pi\rho_0 r}{\lambda_m F}\right)\right] \end{aligned}\Bigg\} \\ &+B_{m+2k}\Bigg\{ \begin{aligned} &\cos(2k\theta)\left[J_{m+2k}\left(\frac{2\pi\rho_0 r}{\lambda_m F}\right) + J_{m-2k}\left(\frac{2\pi\rho_0 r}{\lambda_m F}\right)\right] \\ &+\text{i}\sin(2k\theta)\left[J_{m+2k}\left(\frac{2\pi\rho_0 r}{\lambda_m F}\right) - J_{m-2k}\left(\frac{2\pi\rho_0 r}{\lambda_m F}\right)\right] \end{aligned}\Bigg\} \end{aligned}\Bigg\} \end{aligned}\Bigg\}. \end{aligned} \tag{11}$$

This indicates that these beams are comprised of only one integer OAM phase exp(i$m\theta$), and the Bessel term of $B_m J_m\left(2\pi\rho_0 r/\lambda_m F\right)$ dominates, since B_m is the maximum of B_n. The standing wave terms $\sin\theta\cdot m\lambda_m F B_{m+1}J_m\left(2\pi\rho_0 r/\lambda_m F\right)/\pi\rho_0 r$ and $\cos\theta\cdot B_{m+1}\left[J_{m+1}\left(2\pi\rho_0 r/\lambda_m F\right) - J_{m-1}\left(2\pi\rho_0 r/\lambda_m F\right)\right]$ contribute to the asymmetric intensity of this group of BG beams. In fact, the rest of the B_n factors are really small in comparison with the central term and contribute minimally to the BG beam, but still in the form of standing waves. As shown in Eq. (9), the fractional-charged OAM beams are essentially the combination of integer-charged OAM beams. For each of these integer components, the parameter B_n works as a window to distribute the power between the integer charge OAMs and decays rapidly as parameter n approaches positive and negative infinity.

As can be seen in Eq. (11), a change in β only affects the weighting factor B_n. Conceptually, when β is very small, very little power will be contained at the edges of the active zone on the log polar elements. When this whole area is wrapped, there will be a highly asymmetric ring. As β approaches 1, the distribution about the wrapped ring becomes more azimuthally Gaussian. In fact, as β increases beyond 1, the distribution about the wrapped ring becomes more azimuthally uniform and the weighting factors $B_{l\pm 1}$ decrease, but more of the power will be clipped by the log-polar optic aperture. This results in a lower power efficiency of the system but higher modal symmetry. Equation (9) not only describes the

Optics EXPRESS

distribution of integer charge numbers, but also fractional charge numbers. Figure 2 shows the analytic intensity and phase profiles using simulation parameters λ = 532 nm, β = 0.66, w_{ring} = 329 μm, ρ_0 = 850 μm, using 5 central terms, and for the focal length of Fourier lens F = 400 mm. Due to the small radius of the Gaussian envelope, only one faint ring of the 0th order Bessel-Gaussian beam appears in the simulations and experimental results.

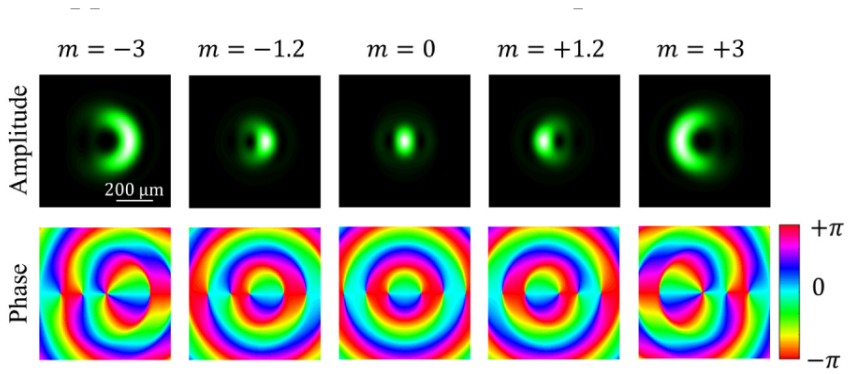

Fig. 2. Analytic intensity and phase profiles for m = ± 3, ± 1.2 and 0.

The log-polar coordinate transform theory assumes that the input is a rectangular shaped beam [20–23]. This notion in fact reduces the translation efficiency of such systems due to the fact that a Fourier transform of a rectangular function contains high spatial frequency components. On the other hand, the Fourier transform of a Gaussian shape produces another Gaussian distribution. In the HOBBIT system presented above, an elliptical Gaussian beam is easily generated from a Gaussian input. This has the added benefit of a higher power efficiency compared to that of a rectangular beam input.

3. Diffractive phase-only optics and experiment setup

3.1 Diffractive phase-only optics

The diffractive log-polar HOBBIT elements are fabricated using a photolithographic method in our cleanroom facility. As shown in Fig. 3(a), 6 row × 6 column devices has been fabricated on a single wafer. The optics are optimized for the wavelength of 532 nm, and have a pixel size of 2 μm × 2 μm and 2^4 = 16 phase levels. The design parameter a is 1.8/π mm and b is 2 mm. The microscope profiles of a wrapper and phase-corrector are shown in Fig. 3(b) and (c). Scanning-electron microscopy (SEM) images of the fabricated optics are shown in Fig. 3(d) and (e) with magnification of 130 ×. The theoretical diffraction efficiency of a 4-layer lithographic process diffractive phase element is about 98%. After applying a 99.9% transmission anti-reflection (AR) coating on each surface of the HOBBIT optics, the mean transmission efficiency of both the wrapper and phase corrector combined has been measured to be 91% with 0.5% standard deviation from charge −10 to 10.

Optics EXPRESS

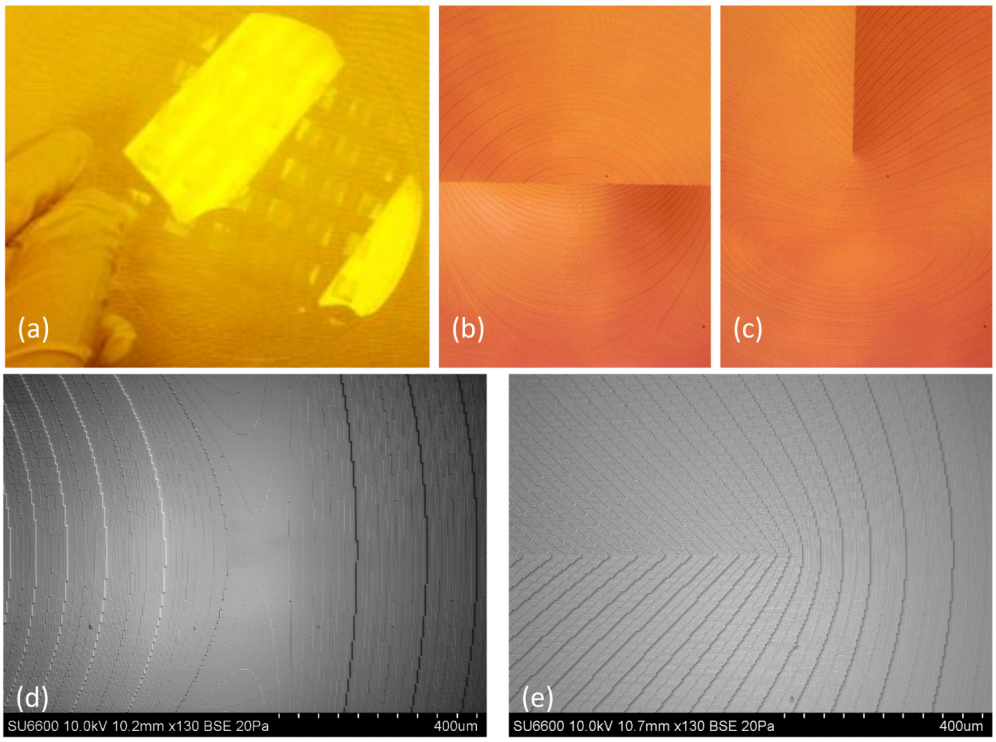

Fig. 3. (a) Multiple log-polar device fabrication on a single wafer, (b) the microscope image of central part of wrapper and (c) phase corrector, (d) the 130 × magnification SEM inspection of device center of wrapper and (e) phase corrector.

3.2 Experiment setup and results

The AOD couples up to 70% of the optical energy into its 1st diffraction order. This deflection angle is continuously tunable by adjusting the frequency of the acoustic signal. As mentioned above, our experimental setup applies a 4-*f* system to image the AOD output deflection angle into the line shape beam's linear phase and another 4-*f* system to elongate the circular Gaussian beam into an elliptical Gaussian beam. The elliptical Gaussian beam is incident upon the wrapper and then is mapped into an azimuthally asymmetric ring shaped beam during propagation to the phase corrector. After phase correction at the second optical element, the ring-shaped beam carrying OAM phase will form a BG beam in the far-field. A diagram of the experimental setup is shown in Fig. 4.

Optics EXPRESS

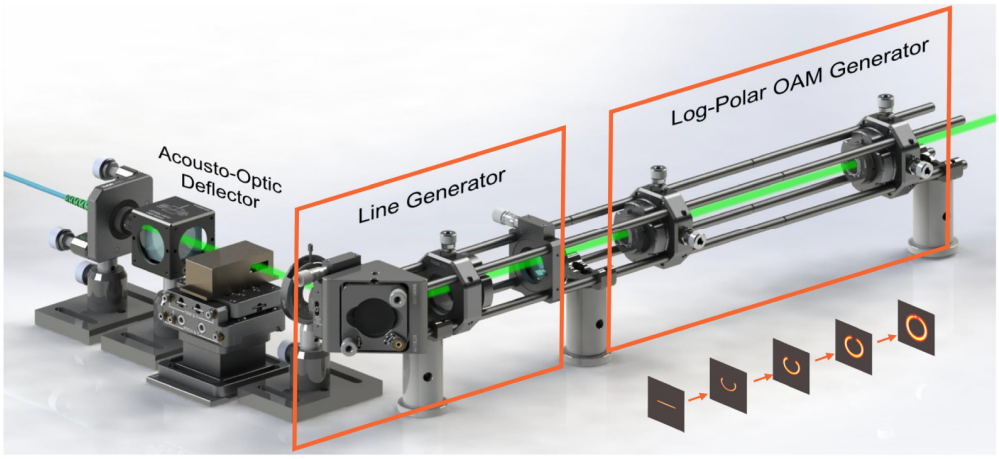

Fig. 4. Diagram of the acousto-optic deflector, line-generator and log-polar transformation optics.

The deflected beam was generated using a Gooch & Housego AODF 4120-3. This AOD is constructed using a tellurium dioxide (TeO_2) crystal, with a Bragg angle of 2.9°, computed by Eq. (1), as shown in Fig. 5. The acoustic velocity is 0.65 mm/μs, typical for the shear mode of a TeO_2 crystal. An input beam with a diameter of approximately 1.5 mm can be deflected at a rate of approximately 434.8 kHz, corresponding to a measured switching speed of 2.3 μs. Higher switching speeds are achievable in other materials such as quartz and fused silica. The acoustic velocity of such devices can be an order of magnitude above the shear-mode TeO_2 devices. By decreasing the beam size through a crystal and with a faster acoustic velocity, switching speeds could be further increased into the tens of megahertz. A picture of the compact experimental setup is shown in Fig. 5. The transmission efficiency of each surfaces of the 3 optics in the line generator is 99%, and the total transmission efficiency of log-polar OAM generator is 91%. Taking into account the 70% AOD's 1st order diffractive efficiency (DE), the total system efficiency is approximately 60%. Given a 30 mW input power, the output BG beam is approximately 18 mW. The current setup is restricted to only one linear polarization due to the requirements of the AOD. However, there are other types of AODs that are polarization insensitive. In this case, different polarization states could be used in the HOBBIT system since the log-polar optics are polarization insensitive.

Optics EXPRESS

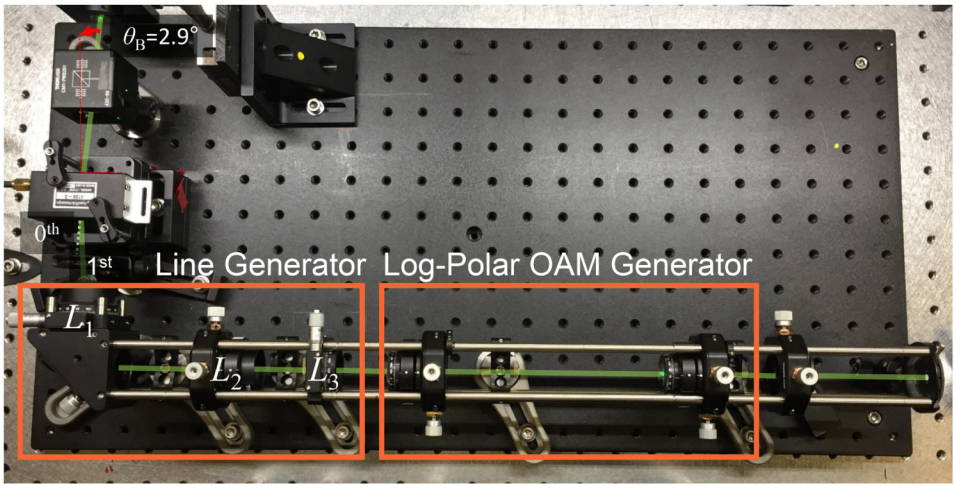

Fig. 5. Picture of the continuously tunable OAM generation system.

The focal lengths L_1 and L_2 are F_1 = 50 mm and F_2 = 100 mm respectively, parameter a = 1.8/π mm, and the frequency index corresponding to Δm = 1 interval is Δf_1 = 0.36 MHz. A series of rings with different OAM phases are output from the log-polar HOBBIT optics. The far-field of this group of ring shape OAM phase carrying beams are BG beams [29]. The generated BG beams are experimental generated, imaged and simulated using Eq. (9) as shown in Fig. 6. The experimental results have good agreement with the simulation results. A comparison of the radius of the dark vortex to the corresponding charge numbers as well as driving signal frequencies is shown in Fig. 7 for both the experimental and simulated beam profiles. This radius was measured by finding the inner radial location of the half-maximum amplitude. The simulation is an approximation of an infinite series. The slight dips in the curve are a result of truncating the infinite series to obtain this approximation. The DE of the m = –5 beam is 8.8% lower than the DE of the m = 5 beam because the deviation away from the Bragg condition that has the highest DE.

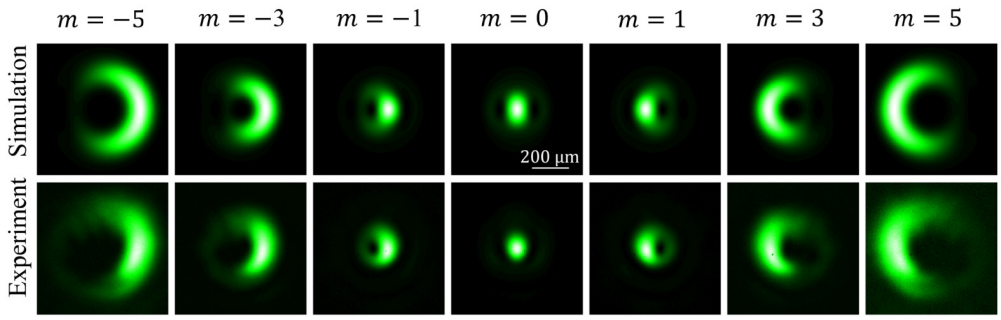

Fig. 6. Comparison of analytic expression with β = 0.663 and ρ_0 = 850 μm.

Optics EXPRESS

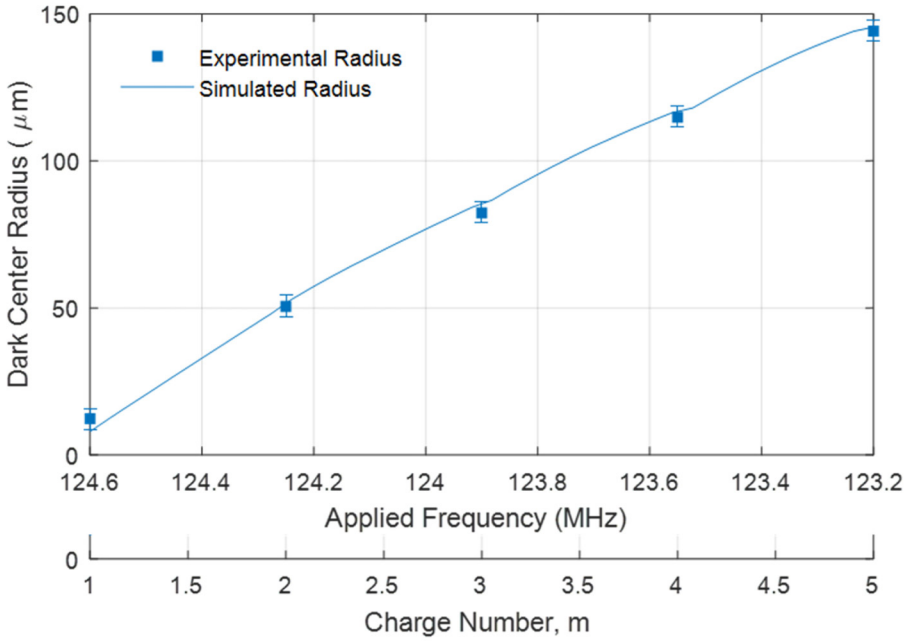

Fig. 7. The simulated and experiment results of BG beams central dark area's radius vary with charge number as well as AOD driving signal's frequency.

The deflection angle of the 1st order AOD output is continuously tunable, therefore the OAM phase is continuously tunable as well. The intensity distributions of the fractional OAM modes spanning from charge −1.2 to + 1.2 in steps of 0.6 are shown in Fig. 8. The charge numbers are verified by the single stationary cylindrical lens method [43–45] as −1.21 ± 0.03, −0.63 ± 0.03, −0.01 ± 0.08, 0.64 ± 0.02 and 1.21 ± 0.02. Two independent methods were used to verify the OAM charge numbers. First, the dark center of the beam intensity was measured and second, a single stationary cylindrical lens method was used. Both independent methods agree and are consistent with the designed OAM charge numbers. See Visualization 1 for a video of the demonstrating scan for charges −3 to + 3 in steps of 0.2.

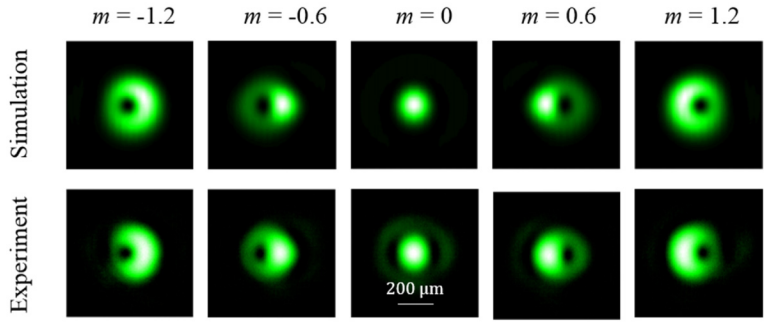

Fig. 8. Experimentally generated and simulated fractional OAM BG beams.

4. Conclusion

In conclusion, we have proposed a method of cascading an AOD with the HOBBIT log-polar transform optical system to rapidly and continuously tune the output OAM mode of a BG beam. This means the HOBBIT system has the capability of generating tunable fractional OAM modes. The OAM mode is controlled through the AOD driving frequency, which

Optics EXPRESS

controls the amount of linear tilt to be wrapped into a ring through the log-polar transformation. The tuning speeds of AODs are limited by the velocity of the acoustic wave through the crystal, which has the potential to well exceed conventional mode manipulators such as DMDs, SLMs, and single electrically contacted thermos-optical controlled vortex emitters. The scalar form of the far-field HOBBIT has been analytically derived, resulting in a group of asymmetric fractional BG beams. See Visualization 1 for a video demonstrating a scan for charges −3 to + 3 in steps of 0.2.

This technique provides a fast and continuous OAM carrying BG beam tuning solution. This HOBBIT system may benefit a multitude of areas not limited to communication from classical to quantum applications, particle optical manipulation, beam shaping, laser beam machining, microscopy, microlithography, direct energy, filamentation, as well as sensing through turbulence in air and underwater environments. OAM is rapidly gaining interest in all of these areas and the tunable capabilities of this system has the potential to open up the in-depth study of these modes under various conditions, including environments that change slowly such as turbulence. Also, the AOD can support a superposition of driving frequencies that result in multiple OAM modes being generated simultaneously. Because of this, future work will consist of exploring coherent combinations of OAM modes from this AOD based HOBBIT system.

5. Appendix

The full derivation of the far field asymmetric Bessel Gaussian beam is presented in this appendix. The near-field output from the proposed HOBBIT system represented by Eq. (8) can be rewritten as separable functions with respect to only ρ or ϕ terms,

$$U_{\text{near}}(\rho,\phi) = \mathrm{P}(\rho)\Phi(\phi), \tag{12}$$

$$\mathrm{P}(\rho) = \exp\left(-\frac{(\rho-\rho_0)^2}{w_{\text{ring}}{}^2}\right), \tag{13}$$

$$\Phi(\phi) = \exp\left[-\frac{\phi^2}{(\beta\pi)^2}\right]\exp(\mathrm{i}m\phi). \tag{14}$$

Since the far field light distribution is the Fourier transform of the near-field, then

$$\begin{aligned} U_{\text{far}}(r,\theta) &= \frac{1}{\mathrm{i}\lambda f}\mathscr{F}\{U_{\text{near}}(\rho,\phi)\} \\ &= \frac{1}{\mathrm{i}\lambda f}\mathscr{F}\left\{\exp\left(-\frac{\rho^2}{w_{\text{ring}}{}^2}\right)\right\}\cdot\mathscr{F}\left\{\delta(\rho-\rho_0)\exp\left[-\frac{\phi^2}{(\beta\pi)^2}\right]\exp(\mathrm{i}m\phi)\right\}. \end{aligned} \tag{15}$$

As shown in Eq. (15), there are two Fourier transforms that need to be solved. It is well known that the Fourier transform of a Gaussian expression is a Gaussian as well. The other Fourier transform term is more interesting and complicated. Starting with the definition of the polar coordinate Fourier transform,

$$U_{\text{far}}(r,\theta) = \frac{1}{\mathrm{i}\lambda f}\int_{-\pi}^{\pi}\int_{0}^{\infty}U_{\text{near}}(\rho,\phi)\exp\left(-\mathrm{i}\frac{2\pi}{\lambda_m F}\rho r\cos(\theta-\phi)\right)\rho d\rho d\phi, \tag{16}$$

the term of interest in Eq. (15) can be written as,

Optics EXPRESS

$$\begin{aligned}&\mathscr{F}\left\{\delta(\rho-\rho_0)\exp\left[-\frac{\phi^2}{(\beta\pi)^2}\right]\exp(\mathrm{i}m\phi)\right\}\\&=\int_{-\pi}^{\pi}\int_{0}^{\infty}\delta(\rho-\rho_0)\exp\left[-\frac{\phi^2}{(\beta\pi)^2}\right]\exp(\mathrm{i}m\phi)\exp\left(-\mathrm{i}\frac{2\pi}{\lambda_m F}\rho r\cos(\theta-\phi)\right)\rho d\rho d\phi.\end{aligned}\tag{17}$$

Appling Jacobi–Anger expansion:

$$\exp\left(-\mathrm{i}\frac{2\pi}{\lambda_m F}\rho r\cos(\theta-\phi)\right)=\sum_{n=-\infty}^{+\infty}(-\mathrm{i})^n J_n\left(\frac{2\pi}{\lambda_m F}\rho r\right)\exp\left[\mathrm{i}n(\theta-\phi)\right].\tag{18}$$

Then Eq. (17) can be re-written as,

$$\begin{aligned}&\mathscr{F}\left\{\delta(\rho-\rho_0)\exp\left[-\frac{\phi^2}{(\beta\pi)^2}\right]\exp(\mathrm{i}m\phi)\right\}\\&=\sum_{n=-\infty}^{+\infty}(-\mathrm{i})^n\exp(\mathrm{i}n\theta)\int_0^{\infty}\delta(\rho-\rho_0)J_l\left(\frac{2\pi}{\lambda_m F}\rho r\right)\rho d\rho\int_{-\pi}^{\pi}\exp\left[-\frac{\phi^2}{(\beta\pi)^2}+\mathrm{i}\phi(m-n)\right]d\phi.\end{aligned}\tag{19}$$

The azimuthal integral can be solved by [46]

$$\begin{aligned}&\int_{-\pi}^{\pi}\exp\left[-\frac{\phi^2}{(\beta\pi)^2}+\mathrm{i}\phi(m-n)\right]d\phi\\&=\frac{-\mathrm{i}\beta\pi\sqrt{\pi}}{2}\exp\left(-\frac{(\beta\pi)^2(m-n)^2}{4}\right)\left[\mathrm{erfi}\left(\mathrm{i}+\frac{\beta\pi(m-n)}{2}\right)-\mathrm{erfi}\left(-\mathrm{i}+\frac{\beta\pi(m-n)}{2}\right)\right]\\&=\beta\pi\sqrt{\pi}\exp\left(-\frac{(\beta\pi)^2(m-n)^2}{4}\right)\mathrm{Im}\left[\mathrm{erfi}\left(\mathrm{i}+\frac{\beta\pi(m-n)}{2}\right)\right].\end{aligned}\tag{20}$$

The far field light distribution in Eq. (15) reduces to the final analytic terms as given by Eq. (9), in which the B_n term is the weighting term and shifts power between different Bessel terms. Considering the $\alpha = 0$ case, given $n = m + k = l + k$, $k = 0, 1, 2\ldots$

$$\begin{aligned}B_{n=l+k}&=(-\mathrm{i})^{l+k-1}\,2\exp\left(-\frac{(\beta\pi)^2(l-(l+k))^2}{4}\right)\mathrm{Im}\left[\mathrm{erfi}\left(\mathrm{i}+\frac{\beta\pi(l-(l+k))}{2}\right)\right]\\&=(-\mathrm{i})^{l+k-1}\,2\exp\left(-\frac{(k\beta\pi)^2}{4}\right)\cdot\mathrm{Im}\left(\mathrm{erfi}\left(\mathrm{i}-\frac{k\beta\pi}{2}\right)\right).\end{aligned}\tag{21}$$

Consider the case of $n = m - k = l - k$,

$$\begin{aligned}B_{n=l-k}&=(-\mathrm{i})^{l-k-1}\,2\exp\left(-\frac{(l-(l-k))^2(\beta\pi)^2}{4}\right)\mathrm{Im}\left[\mathrm{erfi}\left(\mathrm{i}+\frac{(l-(l-k))\beta\pi}{2}\right)\right]\\&=(-\mathrm{i})^{l-k-1}\,2\exp\left(-\frac{(k\beta\pi)^2}{4}\right)\cdot\mathrm{Im}\left(\mathrm{erfi}\left(\mathrm{i}+\frac{k\beta\pi}{2}\right)\right).\end{aligned}\tag{22}$$

The imaginary error function is an odd function, therefore

Optics EXPRESS

$$
\begin{aligned}
B_{n=l-k} &= (-\mathrm{i})^{l-k-1}\, 2\exp\left(-\frac{(k\beta\pi)^2}{4}\right)\cdot \mathrm{Im}\left(\mathrm{erfi}\left(\mathrm{i}+\frac{k\beta\pi}{2}\right)\right) \\
&= \frac{(-\mathrm{i})^{l+k-1}}{(-\mathrm{i})^{2k}}\, 2\exp\left(-\frac{(k\beta\pi)^2}{4}\right)\cdot \mathrm{Im}\left(-\mathrm{erfi}\left(-\mathrm{i}-\frac{k\beta\pi}{2}\right)\right) \\
&= (-1)^k\,(-\mathrm{i})^{l+k-1}\, 2\exp\left(-\frac{(k\beta\pi)^2}{4}\right)\cdot \mathrm{Im}\left(-\mathrm{erfi}\left(\overline{\mathrm{i}-\frac{k\beta\pi}{2}}\right)\right) \\
&= (-1)^k\,(-\mathrm{i})^{l+k-1}\, 2\exp\left(-\frac{(k\beta\pi)^2}{4}\right)\cdot \mathrm{Im}\left(-\overline{\mathrm{erfi}\left(\mathrm{i}-\frac{k\beta\pi}{2}\right)}\right) \\
&= (-1)^k\,(-\mathrm{i})^{l+k-1}\, 2\exp\left(-\frac{(k\beta\pi)^2}{4}\right)\cdot \mathrm{Im}\left(\mathrm{erfi}\left(\mathrm{i}-\frac{k\beta\pi}{2}\right)\right) = (-1)^k\, B_{n=l+k}.
\end{aligned}
\tag{23}
$$

In summary, applying the recurrent property for Bessel functions of the 1st kind, Eq. (9) will reduce into Eq. (11).

Funding

Office of Naval Research (ONR) (N00014-16-1-3090, N00014-17-1-2779).

References

1. M. Chagnon, M. Osman, Q. Zhuge, X. Xu, and D. V. Plant, "Analysis and experimental demonstration of novel 8PolSK-QPSK modulation at 5 bits/symbol for passive mitigation of nonlinear impairments," Opt. Express **21**(25), 30204–30220 (2013).
2. A. J. Willner, Y. Ren, G. Xie, Z. Zhao, Y. Cao, L. Li, N. Ahmed, Z. Wang, Y. Yan, P. Liao, C. Liu, M. Mirhosseini, R. W. Boyd, M. Tur, and A. E. Willner, "Experimental demonstration of 20 Gbit/s data encoding and 2 ns channel hopping using orbital angular momentum modes," Opt. Lett. **40**(24), 5810–5813 (2015).
3. J. Du and J. Wang, "High-dimensional structured light coding/decoding for free-space optical communications free of obstructions," Opt. Lett. **40**(21), 4827–4830 (2015).
4. T. Lei, S. Gao, Z. Li, Y. Yuan, Y. Li, M. Zhang, G. N. Liu, X. Xu, J. Tian, and X. Yuan, "Fast-switchable OAM-based high capacity density optical router," IEEE Photonics J. **9**(1), 1 (2017).
5. N. Radwell, D. Brickus, T. W. Clark, and S. Franke-Arnold, "High speed switching between arbitrary spatial light profiles," Opt. Express **22**(11), 12845–12852 (2014).
6. M. Malik, M. O'Sullivan, B. Rodenburg, M. Mirhosseini, J. Leach, M. P. J. Lavery, M. J. Padgett, and R. W. Boyd, "Influence of atmospheric turbulence on optical communications using orbital angular momentum for encoding," Opt. Express **20**(12), 13195–13200 (2012).
7. M. Krenn, R. Fickler, M. Fink, J. Handsteiner, M. Malik, T. Scheidl, R. Ursin, and A. Zeilinger, "Communication with spatially modulated light through turbulent air across Vienna," New J. Phys. **16**(11), 113028 (2014).
8. C. Ma, X. Xu, Y. Liu, and L. V. Wang, "Time-reversed adapted-perturbation (TRAP) optical focusing onto dynamic objects inside scattering media," Nat. Photonics **8**(12), 931–936 (2014).
9. H. Wang, F. Yuan, S. Chang, P. Sun, S. Zhang, H. Li, Z. Zheng, S. Liu, T. Xie, and C. Wang, "Arbitrary manipulation of micro-particles in three dimensions by steering of multiple orbital angular momentum modes," Proc. SPIE **10347**, 35 (2017).
10. M. P. J. Lavery, F. C. Speirits, S. M. Barnett, and M. J. Padgett, "Detection of a spinning object using light's orbital angular momentum," Science **341**(6145), 537–540 (2013).
11. M. P. J. Lavery, S. M. Barnett, F. C. Speirits, and M. J. Padgett, "Observation of the rotational Doppler shift of a white-light, orbital-angular-momentum-carrying beam backscattered from a rotating body," Optica **1**(1), 1–4 (2014).
12. Z.-Y. Zhou, Y. Li, D.-S. Ding, W. Zhang, S. Shi, and B.-S. Shi, "Optical vortex beam based optical fan for high-precision optical measurements and optical switching," Opt. Lett. **39**(17), 5098–5101 (2014).
13. N. Cvijetic, G. Milione, E. Ip, and T. Wang, "Detecting lateral motion using light's orbital angular momentum," Sci. Rep. **5**(1), 15422 (2015).
14. M. J. Strain, X. Cai, J. Wang, J. Zhu, D. B. Phillips, L. Chen, M. Lopez-Garcia, J. L. O'Brien, M. G. Thompson, M. Sorel, and S. Yu, "Fast electrical switching of orbital angular momentum modes using ultra-compact integrated vortex emitters," Nat. Commun. **5**(1), 4856 (2014).
15. J. Leach, E. Yao, and M. J. Padgett, "Observation of the vortex structure of a non-integer vortex beam," New J. Phys. **6**(1), 71 (2004).
16. J. C. Gutiérrez-Vega and C. López-Mariscal, "Nondiffracting vortex beams with continuous orbital angular

Optics EXPRESS

momentum order dependence," J. Opt. A, Pure Appl. Opt. **10**(1), 015009 (2008).
17. K. Huang, H. Liu, S. Restuccia, M. Q. Mehmood, S. Mei, D. Giovannini, A. Danner, M. J. Padgett, J. Teng, and C. Qiu, "Spiniform phase-encoded metagratings entangling arbitrary rational-order orbital angular momentum," Light Sci. Appl. **7**(3), 17156 (2018).
18. Z. Yang, X. Zhang, C. Bai, and M. Wang, "Nondiffracting light beams carrying fractional orbital angular momentum," J. Opt. Soc. Am. A **35**(3), 452–461 (2018).
19. J. B. Götte, K. O'Holleran, D. Preece, F. Flossmann, S. Franke-Arnold, S. M. Barnett, and M. J. Padgett, "Light beams with fractional orbital angular momentum and their vortex structure," Opt. Express **16**(2), 993–1006 (2008).
20. O. Bryngdahl, "Geometrical transformations in optics," J. Opt. Soc. Am. **64**(8), 1092–1099 (1974).
21. O. Bryngdahl, "Optical map transformations," Opt. Commun. **10**(2), 164–168 (1974).
22. J. Cederquist and A. M. Tai, "Computer-generated holograms for geometric transformations," Appl. Opt. **23**(18), 3099–3104 (1984).
23. M. A. Stuff and J. N. Cederquist, "Coordinate transformations realizable with multiple holographic optical elements," J. Opt. Soc. Am. **7**(6), 977–981 (1990).
24. G. C. G. Berkhout, M. P. J. Lavery, J. Courtial, M. W. Beijersbergen, and M. J. Padgett, "Efficient sorting of orbital angular momentum states of light," Phys. Rev. Lett. **105**(15), 153601 (2010).
25. H. Huang, G. Milione, M. P. J. Lavery, G. Xie, Y. Ren, Y. Cao, N. Ahmed, T. An Nguyen, D. A. Nolan, M.-J. Li, M. Tur, R. R. Alfano, and A. E. Willner, "Mode division multiplexing using an orbital angular momentum mode sorter and MIMO-DSP over a graded-index few-mode optical fibre," Sci. Rep. **5**, 14931 (2015).
26. T. Mhlanga, A. Dudley, A. Mcdonald, F. S. Roux, M. Lavery, M. Padgett, and A. Forbes, "Efficient sorting of Bessel beams," Proc. SPIE **8637**, 86371C (2013).
27. M. Mirhosseini, M. Malik, Z. Shi, and R. W. Boyd, "Efficient separation of the orbital angular momentum eigenstates of light," Nat. Commun. **4**(1), 2781 (2013).
28. I. R. Srimathi, K. Miller, W. Li, K. S. Morgan, J. Baghdady, and E. G. Johnson, "Diffractive orbital angular momentum demultiplexing elements for underwater optical communications," in *Frontiers in Optics* (Optical Society of America, 2016), p. FTh4E.2.
29. W. Li, K. Miller, I. R. Srimathi, Y. Li, K. S. Morgan, and E. G. Johnson, "Efficient 1550 nm diffractive log-polar element based orbital angular momentum mode-division multiplexing," in *Frontiers in Optics* (Optical Society of America, 2017), p. JTu2A.37.
30. G. Ruffato, M. Massari, and F. Romanato, "Compact sorting of optical vortices by means of diffractive transformation optics," Opt. Lett. **42**(3), 551–554 (2017).
31. G. Ruffato, M. Massari, G. Parisi, and F. Romanato, "Test of mode-division multiplexing and demultiplexing in free-space with diffractive transformation optics," Opt. Express **25**(7), 7859–7868 (2017).
32. S. Lightman, G. Hurvitz, R. Gvishi, and A. Arie, "Miniature wide-spectrum mode sorter for vortex beams produced by 3D laser printing," Optica **4**(6), 605–610 (2017).
33. K. S. Morgan, I. S. Raghu, and E. G. Johnson, "Design and fabrication of diffractive optics for orbital angular momentum space division multiplexing," Proc. SPIE **9374**, 93740Y (2015).
34. G. Ruffato, M. Girardi, M. Massari, F. Romanato, E. Mafakheri, and P. Capaldo, "Compact diffractive optics for high-resolution sorting of orbital angular momentum beams," Proc. SPIE **10744**, 18 (2018).
35. W. Akemann, J.-F. Léger, C. Ventalon, B. Mathieu, S. Dieudonné, and L. Bourdieu, "Fast spatial beam shaping by acousto-optic diffraction for 3D non-linear microscopy," Opt. Express **23**(22), 28191–28205 (2015).
36. A. Grinenko, M. P. MacDonald, C. R. P. Courtney, P. D. Wilcox, C. E. M. Demore, S. Cochran, and B. W. Drinkwater, "Tunable beam shaping with a phased array acousto-optic modulator," Opt. Express **23**(1), 26–32 (2015).
37. K. Szulzycki, V. Savaryn, and I. Grulkowski, "Generation of dynamic Bessel beams and dynamic bottle beams using acousto-optic effect," Opt. Express **24**(21), 23977–23991 (2016).
38. V. V. Kotlyar, A. A. Kovalev, and V. A. Soifer, "Asymmetric Bessel modes," Opt. Lett. **39**(8), 2395–2398 (2014).
39. V. V. Kotlyar, A. A. Kovalev, R. V. Skidanov, and V. A. Soifer, "Asymmetric Bessel-Gauss beams," J. Opt. Soc. Am. A **31**(9), 1977–1983 (2014).
40. A. B.-C. Arturo Barcelo-Chong, B. E.-P. Brian Estrada-Portillo, A. C.-B. Arturo Canales-Benavides, and S. L.-A. Servando Lopez-Aguayo, "Asymmetric Mathieu beams," Chin. Opt. Lett. **16**(12), 122601 (2018).
41. G. Ruffato, M. Massari, and F. Romanato, "Diffractive optics for combined spatial- and mode- division demultiplexing of optical vortices: design, fabrication and optical characterization," Sci. Rep. **6**(1), 24760 (2016).
42. G. Ruffato, M. Massari, and F. Romanato, "Compact sorting of optical vortices by means of diffractive transformation optics," Opt. Lett. **42**(3), 551–554 (2017).
43. S. N. Alperin, R. D. Niederriter, J. T. Gopinath, and M. E. Siemens, "Quantitative measurement of the orbital angular momentum of light with a single, stationary lens," Opt. Lett. **41**(21), 5019–5022 (2016).
44. S. N. Alperin and M. E. Siemens, "Angular momentum of topologically structured darkness," Phys. Rev. Lett. **119**(20), 203902 (2017).
45. J. B. Götte, S. Franke-Arnold, R. Zambrini, and S. M. Barnett, "Quantum formulation of fractional orbital angular momentum," J. Mod. Opt. **54**(12), 1723–1738 (2007).
46. I. S. G. and I. M. Ryzhik, *Table of Integrals, Series, and Products* (Academic, 2007).